Inhibition of Metal Dusting of Alloy 800H by Laser Surface Melting

K.T. Voisey, Z. Liu and F.H. Stott
Corrosion and Protection Centre,
School of Materials,
The University of Manchester,
UK.

Abstract

Metal dusting is a catastrophic carburisation phenomenon that occurs at temperatures of 450-850°C in atmospheres of high carbon activity. The resistance of alloys to corrosion, including metal dusting, relies on the formation of a dense, adherent oxide layer that separates the alloy from the corrosive environment. For such an oxide layer to be protective, it must achieve full surface coverage, be crack-free and be established before significant material degradation has occurred. Formation of a protective oxide scale can be enhanced by increasing the population of rapid diffusion paths for the protective elements (e.g. Cr and Al) to reach the alloy surface.

In this work, laser surface melting has been used to improve the metal dusting resistance of Alloy 800H by creating a rapid solidification microstructure and, thereby, increasing the density of rapid diffusion paths. Oxidation during laser processing has been found to be detrimental to metal dusting resistance. However, it has been demonstrated that the resulting oxide can be removed without compromising metal dusting resistance.

Results of exposure to a metal dusting atmosphere (20% H_2 80% CO at 650°C) are presented. Samples have been examined in plan and cross-section using optical and scanning electron microscopy. Selected samples were also examined by electron probe microanalysis and X-ray diffraction.

Introduction

Metal dusting is a catastrophic carburisation phenomenon that occurs at 450-850°C in atmospheres of high carbon activity, conditions typical of methanol, steam reformers and other chemical plants that use synthesis gas (H_2 + CO). All Fe-, Ni- and Co-based alloys are susceptible to metal dusting. The alloys disintegrate into a dust of coke and metal particles, leading to two undesirable effects: metal wastage and coke accumulation.

The generally accepted metal dusting mechanisms are summarised below [1-5]. In Fe-based alloys, carbon deposits on the surface and diffuses into the alloy. The alloy becomes saturated with carbon and cementite, Fe_3C, forms. The presence of cementite restricts carbon ingress. Subsequently, the metastable cementite decomposes into graphite and metal particles. In Ni-base alloys, there is no carbide intermediary; graphite forms directly from the carbon-saturated alloy. Inward growth of graphite disintegrates the alloy. Both these mechanisms lead to the formation of metal particles that catalyse further carbon deposition, promoting further metal dusting attack.

Prevention of diffusion of carbon into the alloy should inhibit metal dusting. A dense, crack-free, adherent scale of alumina or chromia may be a suitable barrier, since carbon is insoluble in these oxides [6]. To create such a scale, sufficient amounts of the scale-forming elements (Cr and/or Al) must either be present at the surface or be able to diffuse to the surface to establish and maintain a protective oxide scale. The empirical relationships developed by Schueler and Schillmoller give a lower limit for the proportions of scale-forming elements required [7].

At the relatively low temperature of metal dusting, diffusion of substitutional solute atoms along grain boundaries and other rapid diffusion paths, such as dislocations, is significant [8]. Therefore, the microstructure and extent of cold work influence the

rate of diffusion and, hence, of scale formation [9]. Inhibition of metal dusting by the use of finer grained alloys [10-12] or cold working [11-14] has been reported.

Two diffusion processes are of interest to this work: diffusion of chromium to the surface to form a protective scale and the inward diffusion of surface adsorbed carbon. It is important to note that chromium is a substitutional solute atom, requiring the presence of vacancies for diffusion. The introduction of microstructural features, such as dislocations or grain boundaries, essentially provides regions with high vacancy concentrations where the lattice is more open and substitutional diffusion is enhanced. However, carbon diffuses as an interstitial solute atom in Fe-base alloys. Since there is already a high probability of empty neighbouring interstitial sites to move to, negligible advantage is gained by an increased density of so-called rapid diffusion paths. Therefore, increasing the density of rapid diffusion paths should enhance the outward diffusion of chromium whilst having negligible effect on the inward diffusion of carbon.

As is well known, rapid solidification produces fine microstructures. Laser irradiation can melt a thin surface layer, generating high thermal gradients. Quenching of this layer by the cooler bulk material causes rapid solidification and, hence, a refined microstructure [15-17]. Due to the increased density of rapid diffusion paths in such refined microstructures, laser surface treatment can promote formation of a protective oxide scale [18].

Paul et al [19] used the radioactive tracer technique to determine experimentally expressions for bulk and grain boundary diffusion of Cr in Alloy 800; their results for D_{bulk} are used in the present calculations. Previous work on the effects of microstructure on diffusion in similar systems includes the use of SNMS (Secondary Neutral Mass Spectroscopy); this provides diffusion coefficients that average out the

effect of differently-orientated grains within the sampled area [9]. The results obtained illustrate the beneficial effects of the presence of additional rapid diffusion paths on the resistance to metal dusting.

Alloy 800H is a Fe-Ni-Cr alloy known to be susceptible to metal dusting [13, 20-23]. The present research uses laser surface melting to refine the microstructure of the alloy surface in order to promote formation of a protective chromia scale, hence inhibiting metal dusting.

Experimental Procedure

Materials

Cubic samples of ~ 1 cm^3 were cut from the supplied Alloy 800H plate. Each face of the sample was ground with 240 grit SiC grinding paper in order to remove the as-received rolled surface and to ensure each surface was equivalent. Reference samples that did not undergo laser treatment were ground to a 600 grit finish prior to exposure. Laser treated samples were subsequently ground with 600 grit SiC in order to remove laser-induced oxides. The composition of Alloy 800H is shown in Table 1.

Laser Treatment

Laser treatment was carried out using a 2 kW CW CO_2 slab laser (ROFIN DC020). X-Y sample motion was achieved by a computer-controlled table. Flowing argon was used as a shield gas to protect the sample surfaces from (excessive) oxidation during treatment.

Reaction tube dimensions constrained the sample sizes to the order of 1 cm. Such samples are large enough to self-quench and induce the desired rapid solidification. However, they are also small enough that effects due to progressive heating of the sample during laser processing can be seen. An 80% overlap was used which resulted

in each point of the surface being laser melted five times. This technique eliminated effects due to progressive sample heating and produced a constant depth for the remelted layer as opposed to the normally observed approximately sinusoidal depth variation that results from a 50% overlap. All six sides of each sample were laser treated in turn, with the same laser processing condition being used for each side of any one sample.

Laser melting of uncoated Alloy 800H was performed using a 40 mm raster, much larger than the sample size, in order to ensure that beam turning occurred well away from the sample and, thus, to avoid generation of hot spots and associated excessive melting.

Initially, laser power (185 W- 2kW) and sample translation velocity (1.5 mm s^{-1} - 200 mm s^{-1}) were varied in order to produce rapidly solidified microstructures with different degrees of microstructural refinement (Figure 2). A beam diameter of ~ 1.5 mm was used with one exception: a 0.5 mm beam diameter was used for the 250 W 1.5 mm s^{-1} condition in an effort to generate a thicker oxide during laser processing. The laser processing parameters selected to treat the samples exposed to the metal dusting environment are given in Table 2.

Metal Dusting Exposure

Samples were located in quartz boats during exposure. Prior to initial exposure samples and quartz boats were ultrasonically cleaned in ethanol and dried by a hot air blast. The quartz boats containing the samples were inserted into the horizontal reaction tube and exposed to a mixed-gas atmosphere of 20% H_2 and 80% CO at 650°C with a flow rate of 50 cm^3 min^{-1}. A double-walled, quartz reaction tube ensured that the reaction gases were mixed and raised to temperature before reaching the

samples. The reaction tube was heated to temperature in flowing H_2. CO was only mixed with the flowing H_2 when the exposure temperature had been reached. After a given exposure time, the CO supply was shut off and the reaction tube cooled to room temperature in flowing H_2.

Sample Examination

At intervals, the exposure to the mixed gas was interrupted, the furnace was cooled and samples were removed, weighed and examined by optical and scanning electron microscopy (SEM). Selected samples were examined by electron probe microanalysis (EPMA) and X-ray diffraction (XRD).

Mass Difference Measurements

Each sample plus quartz boat was weighed prior to exposure. A Sartorius microbalance was used which, with repeated measurements and control samples, can measure to ± 250 μg. The quartz boats, still containing the samples, were removed from the furnace and weighed after the various exposure times. During weighing, samples were not removed from the quartz boats, nor was any carbon deposit cleaned from the samples. The increase in mass was, therefore, a measure of the total mass of carbon deposited on each quartz boat and the specimens it contained, plus any oxygen taken up to form oxide on the sample surfaces.

Results and Discussion

The laser treatment produced an epitaxially solidified microstructure, the depth of which varied from ~ 100 – 500 μm depending on laser processing parameters (Table 2). Microstructural refinement was achieved by cellular solidification within each grain (Figure 1). It should be noted that cellular (non-branching), as opposed to dendritic, solidification occurred. The microstructural feature measured and referred

to as the cell size is the average cell diameter or cell spacing, as distinct from the commonly measured secondary dendrite arm spacing. The cell size depends on the conditions at the solidification front, primarily the cooling rate, GR, the product of the thermal gradient, G, and the solidification rate, R. The cell size increases as the cooling rate decreases [24]. The cell size is also reported to be inversely proportional to the square root of the thermal gradient [25, 26].

Microstructures with a range of average cell sizes (1 μm – 5 μm) were produced by varying the laser power (185 W – 2kW) and translation speed (1.5 mm s^{-1} – 200 mm s^{-1}) (Figure 2). The results have been plotted against the ratio of laser power and velocity as this produces an approximately straight line plot which was useful experimentally. The observed overall trend of average cell size increasing with the ratio of laser power and velocity is as expected from the known dependence of cell size on GR and is consistent with observations made elsewhere for similar processes [27, 28]: for a given velocity, the cell size increases as the power increases, due to the decreased thermal gradient and, hence, decreased cooling rate.

Due to incomplete shielding, some laser-induced oxides were produced during laser processing. The surface was covered with a continuous oxide layer, which, dependent on the laser processing parameters used, generally thickened in discrete locations. XRD showed that Cr_2O_3 and a spinel phase were formed. Laser processing parameters were selected to produce a series of samples with average cell sizes of 1.5, 2.0 and 4.0 μm and different laser-induced oxide scale morphologies (Table 2) which were exposed to the metal dusting environment.

Preliminary experiments showed the presence of such laser-induced oxides to have no beneficial and, possibly, some detrimental effects on the metal dusting resistance of Alloy 800H. This is attributed to the reduction of non-protective Fe-containing spinel

oxides to Fe, which can then catalyse carbon deposition [29]. The laser-induced oxide layer, though continuously covering the surface, was cracked and, hence, did not act as a protective scale.

Laser-induced oxides form on a molten alloy surface that is in continual motion, driven by Marangoni forces. Hence, there was no localised depletion of scale-forming elements beneath this oxide, rather the entire laser-melted layer was slightly, but uniformly, depleted (Figure 3). The extent of this depletion is calculated to be at most 3 %, i.e. Cr content decreased to 18 wt% from 21 wt%, based on assuming a "worst case scenario" of a 30 μm uniformly thick Cr_2O_3 laser-induced oxide formed on a 440 μm laser-melted layer. Removal of the oxide scale did not, therefore, expose material that was depleted significantly in the oxide-forming elements, particularly Cr. The laser-melted samples used in this work were tested after removal of the laser-induced oxide by 600 grit SiC paper; this action also removed the outermost ~ 50 μm of the laser-melted layer.

The formation of carbon deposits occurred rapidly on reference samples of non-treated Alloy 800H; within 100 h, the surface was blackened by carbon and there was widespread growth of carbon filaments, up to ~ 2 mm long (Figure 4a). With further exposure to 221 h, there was an increase in the number of carbon filaments.

The extent of carbon filament growth on the laser surface melted samples was less than that which occurred on non-treated Alloy 800H during a similar exposure time (Figure 5). While there was some scatter in the mass difference results measured for non-treated Alloy 800H (Figure 6), it is clear that the laser treated samples were more resistant to metal dusting than the non-treated Alloy 800H. The 1.5 μm cell size sample gave the best resistance, this is to be expected as this sample has the smallest cell size, and, hence, highest density of rapid diffusion paths. However, the expected

correlation between cell size, i.e. density of rapid diffusion paths, and metal dusting resistance was not evident: the 4.0 μm sample outperformed the 2.0 μm sample. The poor performance of this sample is possibly due to incomplete removal of the laser-induced oxide.

Examination in cross-section of the exposed samples revealed severe uniform attack on one face of the 250 W sample, and no individual pits could be distinguished. Four distinct pits were observed on the 730 W sample and only one on the 1.5 kW sample. Each of the four pits on the 730 W sample were within the laser-melted layer whereas the pit on the 1.5 kW sample penetrated into the underlying bulk material (Figure 7a and b). However, it should be noted that these observations were each from a single cross-section that did not necessarily pass through the mid point of the pit. Further measurements are needed before quantitative assessments of put densities and sizes can be made. A thin, ~ 1 μm, thermally grown oxide layer was observed on the surface of each sample (Figure 7c and Figure 8b).

The benefit of laser surface treatment can be seen in the EPMA elemental profiles (Figure 8). No evidence of a protective oxide scale was observed on the non-treated Alloy 800H whereas a thermally grown Cr-rich surface oxide scale, and associated depletion profile for Cr in the alloy, can be seen on the laser-treated material. However, numerous EPMA profiles have also shown that such an oxide scale is not present over the entire sample surface, indicating incomplete protection of the alloy.

Quantitative EPMA spot analyses were used to calibrate the linescans. The average Cr concentration in the laser-treated layer, $C_{L,}$ and at the alloy / oxide scale interface, C_I were determined from EPMA linescans. Fitting of the depletion profiles to Eqn (1), where z is the distance from the metal / oxide scale interface and t is the exposure time, allowed the effective diffusion coefficient, D_{eff}, of Cr to be determined.

$$C(z,t) = (C_L - C_I)erf\left(\frac{z}{2\sqrt{D_{eff}t}}\right) + C_L \qquad \text{Eqn (1)}$$

Hart's expression [30] was then used to determine the cell boundary diffusion coefficient, D_{cb}, as shown in Eqn (2):

$$D_{eff} = D_{bulk}(1-f) + D_{cb}f \qquad \text{Eqn (2)}$$

$$f = \frac{2\partial}{g} \qquad \text{Eqn (3)}$$

where, f, is the fractional area occupied by cell boundaries. This was calculated (Eqn 3) by assuming square cells of edge length, g, and assigning 0.5 nm as the width of the cell boundaries, δ, a value previously used for similar work in the open literature [9, 19]. Eqn (3) takes account of the fact that each grain boundary is shared between two grains and it was assumed that $g >> \delta$. Following the work of Paul et al on diffusion of Cr in Alloy 800 [19], a value of 1.76×10^{-20} m^2 s^{-1} was used for the bulk diffusion coefficient, D_{bulk}.

Results from analysis of the observed depletion profiles are shown in Table 3. The measured values of C_I and C_L have been inserted into Eqn (1). The Cr profile predicted by this equation was fitted to that experimentally determined by varying the values of D_{eff}. The actual value of D_{eff} reported for each laser condition is that which gave the best fit to the experimentally-observed profile. In each case, D_{eff} is significantly larger than the literature value of D_{bulk}, indicating that the laser- refined microstructure has had the desired effect on the diffusion characteristics of the alloy.

The fractional area occupied by cell boundaries, f, increases in inverse proportion to the cell size (Eqn 3). Cell boundaries are rapid diffusion paths, i.e. $D_{cb} >> D_{bulk}$; therefore, D_{eff} is expected to increase with decreasing cell size (Eqn 2). However, this

was not observed. Repeated EPMA scans on the 2.0 μm sample produced calculated values of D_{eff} which varied over two orders of magnitude.

As seen in Figure 1, the angle between the cell axis and the sample surface can vary by up to at least 45°. This would decrease the density of intersections between cell boundaries and the surface, thereby decreasing the density of rapid diffusion paths to 70 % of the maximum value, which would occur when the cell boundaries are perpendicular to the sample surface. However, such an effect cannot explain the extent of variation observed.

The procedure used to determine D_{eff} actually fits the product ($D_{eff} \times t$) to the experimentally-measured Cr depletion profiles. This approach assumed that the oxide scale examined was growing from the beginning of the exposure. However, if there was a delay before nucleation of the oxide, a smaller value of t would be appropriate, due to the shorter length of time during which the scale had been growing. Therefore, for the results presented above, an artificially high value for t may have been used, resulting in an artificially low value of D_{eff}. The error introduced by this effect would be greater for later nucleating and, hence, thinner scales, where the scale growth time would be a smaller fraction of the exposure time. Hence, if such a nucleation effect is relevant, the calculated values of D_{eff} would be smaller for thinner scales.

A plot of calculated D_{eff} values against the measured half scale thickness for the repeated EPMA scans performed on the same, 2.0 μm sample, does show such a correlation. The large variation in D_{eff} results obtained is, therefore, attributed to this nucleation effect.

The half scale thickness is measured from the Cr peak in the thermally grown scale to the trough of the Cr depletion profile which corresponds to the metal/oxide scale

interface. This measurement is used in preference to the scale thickness as it can be difficult to determine accurately the location of the outer surface of the scale from the EPMA elemental profiles.

To obtain the true value of D_{eff}, such a nucleation effect needs to be minimised. This would be possible using longer exposure times, so that the delay until nucleation became negligible. Another method would be to expose the samples in conditions where there is a higher partial pressure of oxygen. Though this would move away from metal dusting conditions, results from the study of the effect of the laser-treated microstructure would still be of relevance to the inhibition of metal dusting.

Conclusions

1. The metal dusting resistance of Alloy 800H has been successfully improved by laser surface melting.

2. Laser surface melting creates a refined microstructure that increases the effective diffusion coefficient for Cr in the alloy by introducing a higher density of rapid diffusion paths and, hence, promoting formation of a protective oxide scale.

3. The extent of microstructural refinement can be controlled by varying laser processing parameters.

4. Laser-induced oxidation is detrimental to metal dusting resistance due to reduction of Fe-containing oxides. However, since laser-induced oxides form with no underlying depletion layer, they may be removed without compromising metal dusting resistance.

5. A nucleation effect is proposed to account for the large variation in D_{eff} values determined by repeated examination of a single sample.

Acknowledgements

The authors are grateful to the Engineering and Physical Sciences Research Council for support of this project and to Special Metals Wiggin Ltd., particularly S. McCoy, and Synetix, particularly J.A. Richardson, for support and advice. Mr D. Moore should be thanked for assisting with SEM work.

References

[1] Szakálos, P. and L. Liu. (2002) Mechanisms of Metal Dusting - Application to Alloy Composition, Temperature and Pressure, in Proceedings of 15th International Corrosion Congress "Frontiers in Corrosion Science and Technology", Granada, Spain.

[2] Grabke, H.J., (1998) Thermodynamics, Mechanisms and Kinetics of Metal Dusting, Materials & Corrosion 49, 303-308.

[3] Schneider, R., E. Pippel, J. Woltersdorf, S. Strauss, and H.J. Grabke, (1997) Microprocesses of Metal Dusting on Nickel and Ni-base Alloys, Steel Research 68, 326-332.

[4] Hochman, R.F. (1966) Metal Deterioration in Carbon Monoxide and Hydrocarbon at Elevated Temperatures, in Proceedings of 3rd International Congress on Metallic Corrosion, Moscow, USSR.

[5] Pippel, E., J. Woltersdorf, and R. Schneider, (1998) Micromechanisms of Metal Dusting on Fe-Base and Ni-Base Alloys, Materials & Corrosion 49, 309-316.

[6] Wolf, I. and H.J. Grabke, (1985) A Study on the Solubility and Distribution of Carbon in Oxides, Solid State Communications 54, 5-10.

[7] Jones, R.T. and K.L. Baumert. (2001) Metal Dusting - an Overview of Current Literature, in Proceedings of Corrosion 2001, Paper 01372, National Association of Corrosion Engineers, Houston, Texas.

[8] Porter, D.A. and K.E. Easterling, (1992) Phase Transformations in Metals and Alloys, Chapman & Hall.

[9] Ostwald, C. and H.J. Grabke, (2004) Initial Oxidation and Chromium Diffusion. I. Effects of Surface Working on 9-20% Cr Steels, Corrosion Science 46, 1113-1127.

[10] Han, G.W., D. Feng, and B. Deng, (2004) Metal Dusting and Coking of Alloy 803, Corrosion Science 46, 443-452.

[11] Hänsel, M., C.A. Boddington, and D.J. Young, (2003) Internal Oxidation and Carburisation of Heat-Resistant Alloys, Corrosion Science 45, 967-981.

[12] Grabke, H.J., E.M. Müller-Lorenz, S. Strauss, E. Pippel, and J. Woltersdorf, (1998) Effects of Grain Size, Cold Working, and Surface Finish on the Metal-Dusting Resistance of Steels, Oxidation of Metals 50, 241-254.

[13] Maier, M., J.F. Norton, and P. Puschek, (2000) A Study of the Factors Contributing to the Metal Dusting of Fe-Cr-Ni Alloys in Highly Carburising Atmospheres, Materials at High Temperatures 17, 347-354.

[14] Piehl, C., Z. Toekei, and H.J. Grabke, (2000) Influence of Chromium Diffusion and Different Surface Finishes on the Oxidation Behaviour of Chromium Steels, Materials at High Temperatures 17, 243-246.

[15] Carboni, C., P. Peyre, G. Beranger, and C. Lemaitre, (2002) Influence of High Power Diode Laser Surface Melting on the Pitting Corrosion Resistance of Type 316L Stainless Steel, J Materials Science 37, 3715-3723.

[16] Lomaev, G.V. and E.V. Kharanzhevskii, (2002) Hardening Surface Treatment by the Method of High-Speed Laser Recrystallization, Metal Science and Heat Treatment 44, 128-132.

[17] Strutt, P.R., (1981) Microstructural Refinement of Hard Iron Base Materials by Laser and Electron Beam Surface Modification, Metals Forum 4, 117-123.

[18] Stokes, P.S.N., F.H. Stott, and G.C. Wood, (1989) The Influence of Laser Surface Treatment on the High-Temperature Oxidation of Cr_2O_3-forming Alloys, Materials Science & Engineering A 121, 549-554.

[19] Paul, A.R., K.N.G. Kaimal, M.C. Naik, and S.R. Dharwadkar, (1994) Lattice and Grain Boundary Diffusion of Chromium in Superalloy Incoloy-800, J Nuclear Materials 217, 75-81.

[20] Toh, C.H., P.R. Monroe, and D.J. Young. (2002) Metal Dusting of Heat Resistant Alloys, in Proceedings of 15th International Corrosion Congress "Frontiers in Corrosion Science and Technology", Granada, Spain.

[21] Klarstrom, D.L., H.J. Grabke, and L.D. Paul. (2001) The Metal Dusting Behavior of Several High Temperature Nickel Based Alloys, in Proceedings of Corrosion 2001, Paper 01379, National Association of Corrosion Engineers, Houston, Texas.

[22] Grabke, H.J., (2000) Nickel-Based Alloys in Carbonaceous Gases, Corrosion 56, 801-808.

[23] Grabke, H.J. and E.M. Muller-Lorenz. (2001) Occurrence and Prevention of Metal Dusting on Stainless Steels, in Proceedings of Corrosion 2001, Paper no. 01373, National Association of Corrosion Engineers, Houston, Texas.

[24] Flemings, M.C., (1974) Solidification Processing, McGraw-Hill Inc.

[25] Steen, W.M., (2001) Laser Material Processing, Springer-Verlag.

[26] Phanikumar, G. and K. Chattopadhyay, (2001) Solidification Microstructure Development, Sadhana 26, 25-34.

[27] Kwok, C.T., K.H. Lo, F.T. Cheng, and H.C. Man, (2003) Effect of Processing Conditions on the Corrosion Performance of Laser Surface-Melted AISI 440C Martensitic Stainless Steel, Surface & Coatings Technology 166, 221-230.

[28] Strutt, P.R., (1980) A Comparative Study of Electron Beam and Laser Melting of M2 Tool Steel, Materials Science and Engineering 44, 239-250.

[29] Hochman, R.F. (1972) Basic Studies of Metal Deterioration ("Metal Dusting") in Carbonaceous Environments at Elevated Temperatures, in Proceedings of 5th Metallic Corrosion Conference, 258-263.

[30] Kirkaldy, J.S. and D.J. Young, (1987) Diffusion in the Condensed State, The Institute of Metals.

Tables

	Al	C	Co	Cr	Cu	Fe	Mn	Mo	Nb	Ni	S	Si	Ti	P
Alloy 800H	0.22	0.067	0.06	19.67	0.16	45.34	0.76	0.29	0.02	33.05	<0.001	0.08	0.27	0.012

Table 1 Composition (wt%) of Alloy 800H, as supplied by the manufacturers for the specific batch of material used.

Power (W)	Velocity (mm s^{-1})	Beam diameter (mm)	Power density (W cm^{-2})	Melt depth (μm)	Oxide morphology	Cell size (μm)
1500	100	1.5	8.49×10^4	135	discrete 8 μm continuous 2 μm	1.5 ± 0.4
250	1.5	0.5	1.27×10^5	225	continuous 13 μm	2.0 ±0.4
730	12.5	1.5	4.13×10^4	440	discrete 63 μm continuous 12 μm	4.0 ± 0.5

Table 2 Summary of the laser processing conditions used in this work.

Laser conditions	Cell size (μm)	D_{eff} (m^2 s^{-1})	D_{cb} (m^2 s^{-1})
730W 12.5 mm s^{-1}	4.0 ± 0.5	1.8×10^{-18}	7.13×10^{-15}
250W 1.5 mm s^{-1}	2.0 ± 0.4	2.5×10^{-18}	4.96×10^{-15}
1.5kW 100 mm s^{-1}	1.5 ± 0.4	5.0×10^{-19}	7.24×10^{-16}

Table 3 Experimentally-determined effective and cell boundary diffusion coefficients.

Figure legends

Figure 1 Rapid solidification microstructure generated by laser surface melting of Alloy 800H (1.5 kW 100 mm s^{-1}).

Figure 2 Solidification cell size as a function of laser processing parameters for a beam size of 1.5 mm.

Figure 3 EPMA elemental profile of laser induced oxide and underlying laser-melted layer. Alloy 800H, 250 W, 1.5 mm s^{-1}.

Figure 4 Non-laser treated Alloy 800H, (a) 96 h (b) 221 h.

Figure 5 Laser-treated samples after 185 h. Measured cell sizes are as indicated.

Figure 6 Measured mass differences for laser-treated Alloy 800H.

Figure 7 SEM micrographs of samples of laser-treated Alloy 800H after 329 h exposure to the carbon-containing gas at 650°C (a) 730 W 12.5 mm s^{-1} (b & c) 1.5 kW 100 mm s^{-1}.

Figure 8 EPMA elemental profiles for Alloy 800H (a) non-treated (b) laser treated, 1.5kW 100 mm s^{-1}.

Figure 9 Correlation between the calculated effective diffusion coefficient and scale thickness.

Figures

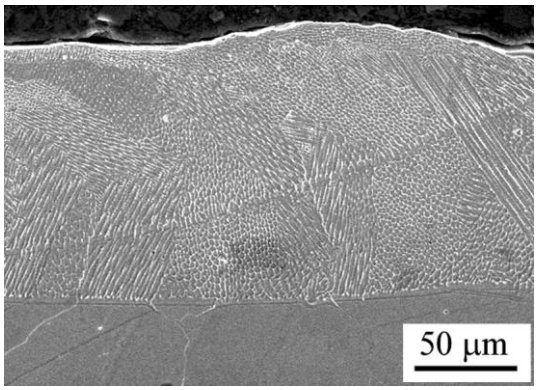

Figure 1 Rapid solidification microstructure generated by laser surface melting of Alloy 800H (1.5 kW 100 mm s^{-1}).

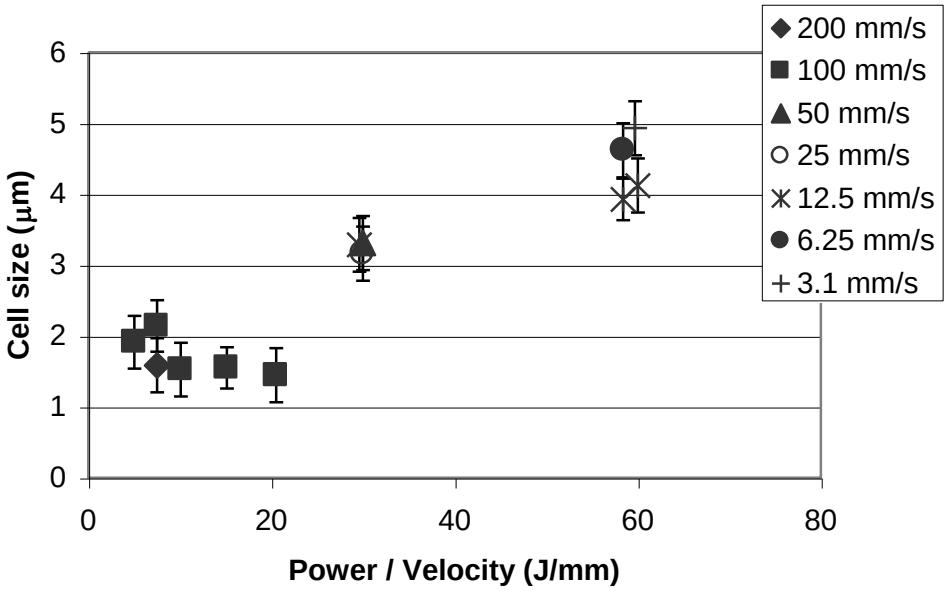

Figure 2 Solidification cell size as a function of laser processing parameters for a beam size of 1.5 mm.

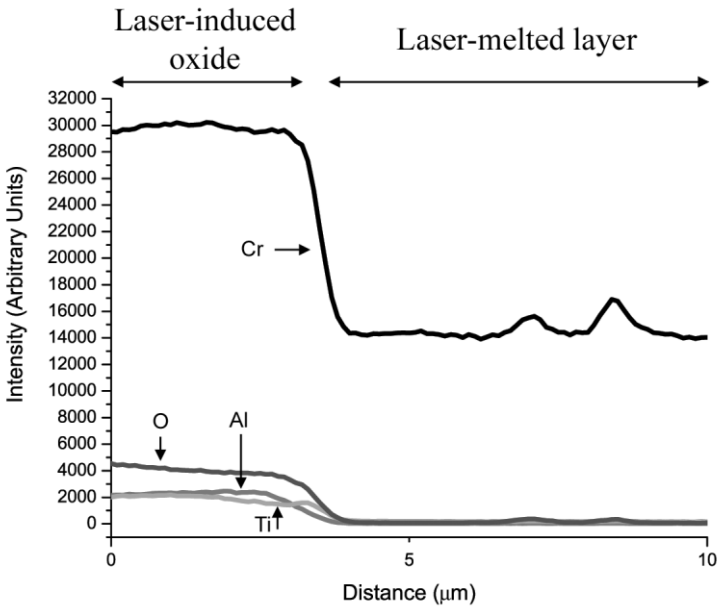

Figure 3 EPMA elemental profile of laser induced oxide and underlying laser-melted layer. Alloy 800H, 250 W, 1.5 mm s^{-1}.

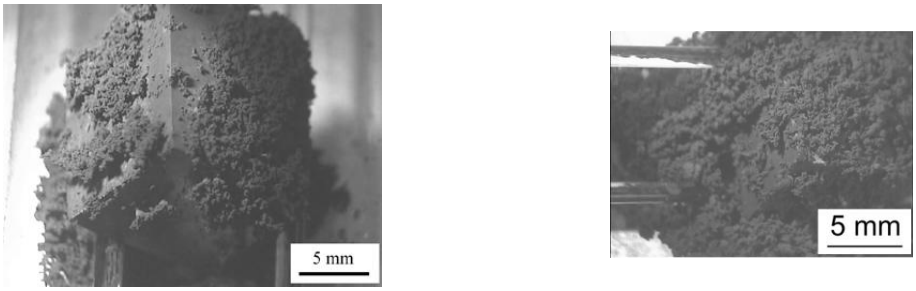

(a) (b)

Figure 4 Non-laser treated Alloy 800H, (a) 96 h (b) 221 h.

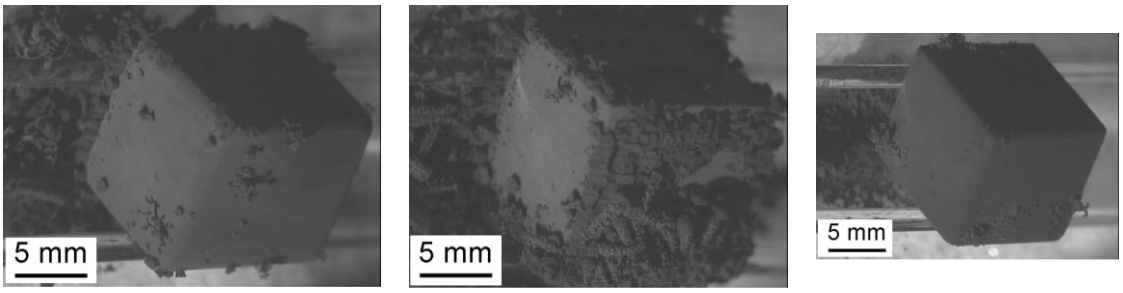

4.0 μm ± 0.5 2.0 μm ± 0.4 1.5 μm ± 0.4

Figure 5 Laser-treated samples after 185 h. Measured cell sizes are as indicated.

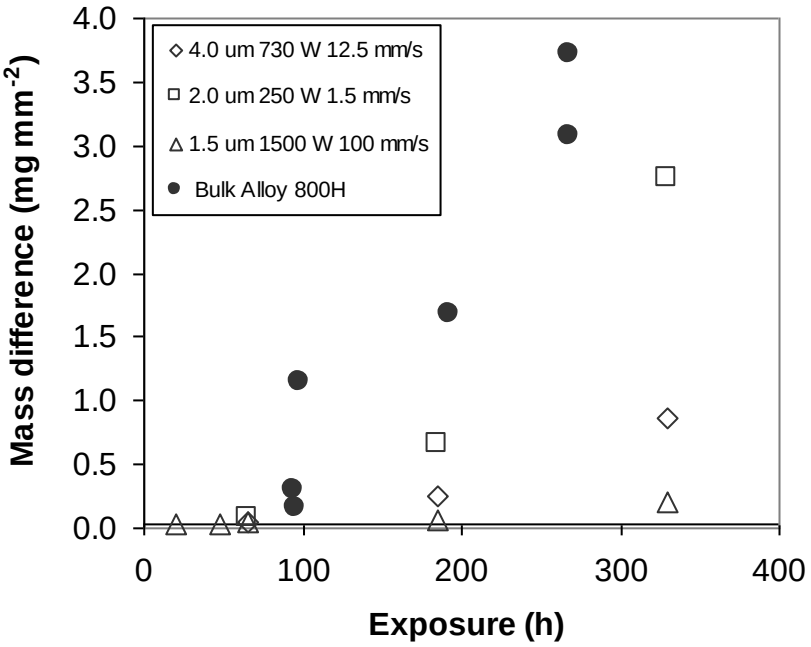

Figure 6 Measured mass differences for laser-treated Alloy 800H.

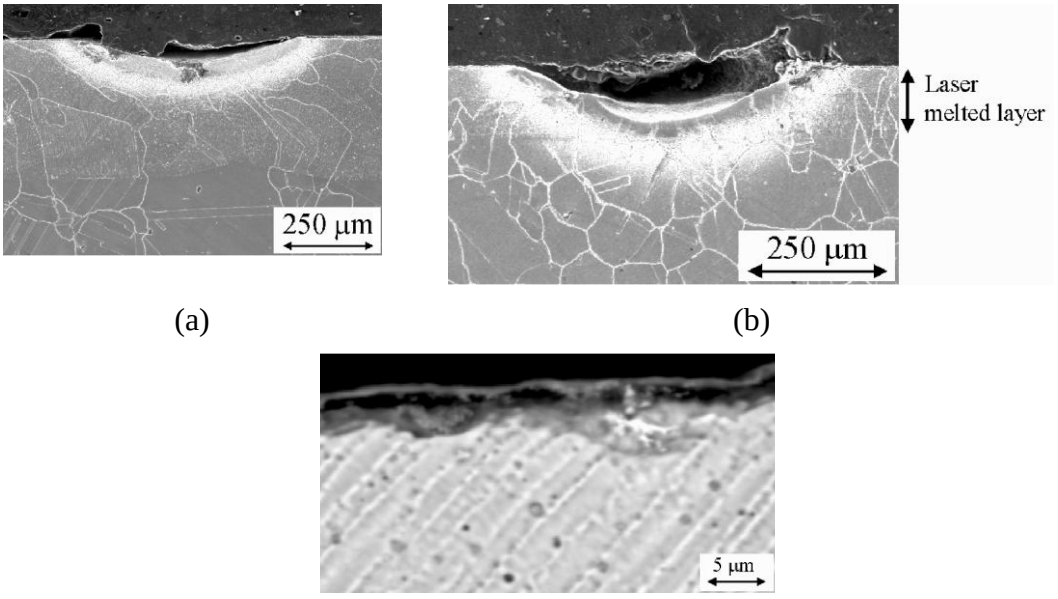

(a) (b)

(c)

Figure 7 SEM micrographs of samples of laser-treated Alloy 800H after 329 h exposure to the carbon-containing gas at 650°C (a) 730 W 12.5 mm s^{-1} (b & c) 1.5 kW 100 mm s^{-1}.

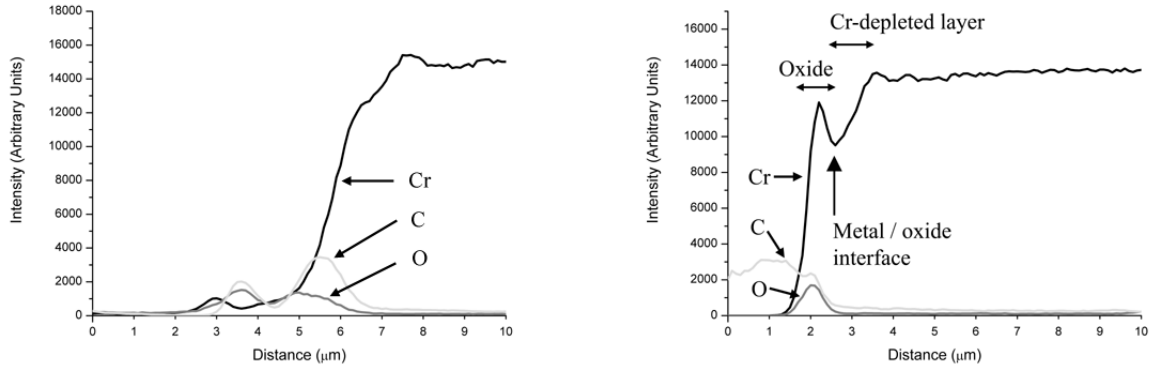

(a) (b)

Figure 8 EPMA elemental profiles for Alloy 800H (a) non-treated (b) laser treated, 1.5kW 100 mm s^{-1}.

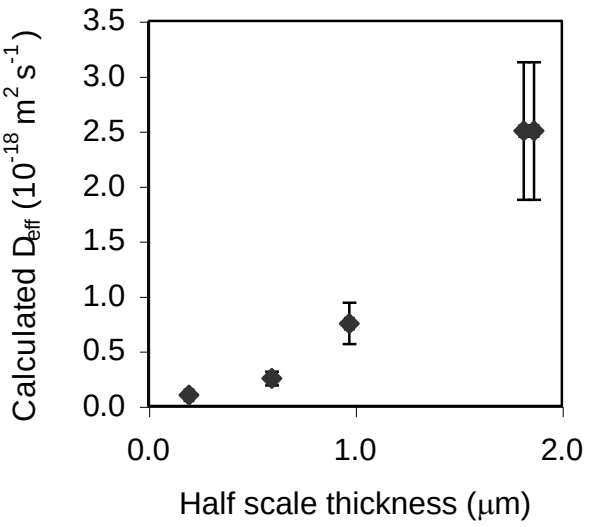

Figure 9 Correlation between the calculated effective diffusion coefficient and scale thickness.